



Pin-Hole Array Correlation Imaging: Highly Parallel Fluorescence Correlation Spectroscopy

Citation

Needleman, Daniel J., Yangqing Xu, and Timothy J. Mitchison. 2009. Pin-hole array correlation imaging: Highly parallel fluorescence correlation spectroscopy. *Biophysical Journal* 96(12): 5050-5059.

Published Version

doi:10.1016/j.bpj.2009.03.023

Permanent link

<http://nrs.harvard.edu/urn-3:HUL.InstRepos:9949288>

Terms of Use

This article was downloaded from Harvard University's DASH repository, and is made available under the terms and conditions applicable to Other Posted Material, as set forth at <http://nrs.harvard.edu/urn-3:HUL.InstRepos:dash.current.terms-of-use#LAA>

Share Your Story

The Harvard community has made this article openly available.
Please share how this access benefits you. [Submit a story](#).

[Accessibility](#)

Pin-Hole Array Correlation Imaging: Highly Parallel Fluorescence Correlation Spectroscopy

Daniel J. Needleman, Yangqing Xu, Timothy J. Mitchison

Department of Systems Biology, Harvard Medical School, Boston, Massachusetts

Key Words

fluorescence correlation spectroscopy, spinning disk confocal, image correlation spectroscopy, electron multiplying charge coupled detector, Nipkow disk, FOXO

ABSTRACT

In this paper we describe pin-hole array correlation imaging (PACI), a multi-point version of fluorescence correlation spectroscopy (FCS), based upon a stationary Nipkow disk and a high speed electron multiplying charged coupled detector. We characterize the system and test its performance on a variety of samples including 40 nm colloids, a fluorescent protein complex, a membrane dye, and a fluorescence fusion protein. Our results demonstrate that PACI is capable of simultaneously performing tens or hundreds of FCS-style measurements in cells, with sufficient sensitivity and temporal resolution to study the behaviors of membrane-bound and soluble molecules labeled with conventional chemical dyes or fluorescent proteins.

INTRODUCTION

Fluorescence Correlation Spectroscopy (FCS) is a powerful technique for studying the dynamics of fluorescently labeled molecules. In a standard FCS experiment, a setup with a configuration similar to a laser scanning confocal microscope is used to measure intensity fluctuations from a diffraction limited volume in a sample. The temporal autocorrelation function of these fluctuations are computed and compared to predictions from a model of the physical processes underlying the systems dynamics [1]. While FCS has many applications [2], it has generated particular excitement because it is one of the few techniques capable of quantitatively measuring concentrations, diffusion coefficients, and binding constants of labeled molecules in cells.

One of the limitations of standard implementations of FCS is that the sample is only probed at a single diffraction limited spot. Therefore, studying heterogeneous samples can be difficult since many individual measurements must be performed at different locations. This drawback is particularly severe in biological applications because the spatial regulation of biochemical activities are crucial for cellular behaviors [3].

A wide variety of methods have been developed to expand the number of spatial locations that can be conveniently probed by fluorescence correlation based techniques. The conceptually simplest forms of spatially extended FCS use two separate diffraction limited volumes in the same sample [4, 5]. Alternatively, a single laser beam can be repetitively scanned across the sample in a linear or circular pattern [6, 7]. Even more spatial locations can be probed using Image Correlation Spectroscopy (ICS); a suite of related techniques based on computing correlation functions from series of images [8]. ICS is most frequently implemented with images collected by one- [9] or two-photon [10] laser scanning confocal microscopy - which make use of a point detector and a fast scanning laser - but is limited to studying relatively slow dynamics with a time scale of hundreds of milliseconds.

Recently, a number of groups have performed ICS type analysis using area detectors, allowing truly parallel data collection. Back-illuminated electron multiplying charge coupled devices (EMCCD) are excellent cameras for such applications because of their high quantum efficiency, high speed, and low noise. EMCCDs have been used in conjunction with standard confocal optics to perform FCS style measurements [11, 12], but it is difficult to create more than a couple of confocal volumes with this method.

Sisan, et al showed that tens of thousands of independent locations can be simultaneously probed using an EMCCD with Spinning Disk Confocal Microscopy (SDCM) for ICS [13]. A SDCM contains two connected disks, one with an array of microlenses to focus laser light onto the sample, the other with an array of aligned pinholes which create the confocal volumes [14]. These disks are rapidly spun so that an entire confocal image is created and can be imaged with a camera. Two disadvantages of SDCM for ICS applications are: 1) The acquisition speed is limited to ~1,000 frames per second by the speed of rotation of the disks and 2) The pinholes only take up a small area of the disk, so any given pixel on the camera only receives light from the sample for a short fraction of the exposure time. The resulting decrease in measured intensity leads to a lower apparent particle brightness, greatly reducing the signal-to-noise ratio. This second drawback limited the applicability of SDCM correlation techniques to ~200 nm fluorescent spheres, which were estimated to have a molecular brightness equivalent to one hundred thousand fluorophores [13]. These two disadvantages can be avoided if Total Internal Reflection Microscopy (TIRFM) illumination is used instead of SDCM. ICS performed with TIRFM and EMCCDs has been used to measure the diffusion of dye molecules in lipid bilayers [15] and the diffusion of fluorescent proteins in cell membranes [15, 16]. However, TIRFM can only be used to study the dynamics of molecules within a few hundred nanometers from the coverslip, greatly limiting its applicability.

In this article we show that if a SDCM is prevented from spinning, it can be used in conjunction with high-powered laser excitation and an EMCCD to simultaneously perform tens or hundreds of FCS type measurements on soluble fluorescently labeled proteins in cells. This technique, which we call Pin-hole Array Correlation Imaging (PACI), is an intermediate between FCS and ICS: The time resolution of PACI is ten to hundred times slower than FCS performed with point detectors, but there is a concurrent increase in the number of spatial locations probed. Conversely PACI interrogates fewer points than is possible with SDCM ICS, but has an increased speed and sensitivity. Unlike TIRFM, PACI can be used to investigate the dynamics of molecules away from the coverslip. While the imaging speed used in the current implementation of PACI is not fast enough to measure the diffusion of free dye molecules in water, we demonstrate its utility on a variety of samples including 40 nm fluorescent colloids, R-Phycoerythrin (a protein complex), a fluorescent dye incorporated into cell membranes, and a soluble fluorescent protein in cells. We believe that PACI has considerable promise as a tool for cell biology, because it is capable of measuring the concentration and diffusion coefficients of chemically and genetically labeled soluble proteins at tens or hundreds of points in cells; and it is easily implemented.

MATERIALS AND METHODS

PACI

A schematic of the experimental system is depicted in Figure 1. Measurements were performed on a Nikon TE2000 inverted microscope with a Yokogawa CSU10 spinning disk confocal head and an EMCCD (iXon 860, Andor, with 128x128 pixels). A 100x oil immersion objective (1.4 NA) was used and the imaging depth was normally within five microns from the coverslip.

An 80mW, 491 nm solid state laser (Cobolt Calypso 100) and a 60 mW, 560 nm solid state laser (Cobolot Jive 75) were directed to an AOTF (NEOS) that was controlled using the Metamorph software package (Molecular Devices). The total power at the sample ranged from 1.5 mW to 200 μ W, depending on the sample under investigation. This power output was split over \sim 1000 pinholes, resulting in 1.5-0.2 μ W per location. This laser power per pinhole is quite low compared to values typically used in FCS experiments [17] and little bleaching was observed - as determined by a lack of decrease in particle number or average intensity during measurements (data not shown).

The optical setup is similar to that used for imaging applications of spinning disk confocal microscopy [18], with two modifications: 1) In the CSU10, a safety shutter normally prevents laser excitation when the motor is not spinning. Yokogawa kindly provided a custom built switch that enabled the motor to be turned on and off while the safety shutter is open. Alternatively, the laser shutter can be disabled by manually removing the shutter or it can be overridden with the pin controller. While similar procedures could be used for the CSU22, they are reportedly not necessary for the CSU-X1. The shutter in the CSU-X1 stays open when the unit is turned off, so simply tuning off the unit is all that is required. 2) The sensor in the iXon 860 is only \sim 3 mm x \sim 3 mm enabling a maximum of \sim 100 pinholes to be imaged. Demagnifying optics - with a net 0.67x or 0.35x - were placed between the EMCCD and the spinning disk confocal head allowing hundreds of additional pinholes to be imaged.

The EMCCD was controlled with Andor's SOLIS software package. The sensor was cooled to -80 C. The maximum gain was selected that did not result in saturation and the baseline clamp was always enabled. Exposure time varied from 0.3 ms to 1.98 ms, depending on the size of the region of interest (and thus the number of pinholes). With full frames, over six hundred individual pinholes could be acquired at a speed of \sim 500 frames per second. Imaging speed increases with decreasing number of horizontal rows read out, and \sim 100 pinholes could be investigated at \sim 1,500 Hz and \sim 10 pinholes at \sim 3,300 Hz.. Greater speeds can also be achieved by binning, but this was not normally used. Movies 40,000 frames long were streamed to RAM or a RAID array. Typically, 3-10 movies were taken per sample.

Analysis

Images were converted to individual TIFFs and analyzed offline using custom written MatLab code. Pictures were loaded and the locations of pinholes was automatically identified using standard particle tracking procedures [19] implemented with freely available Matlab code (<http://physics.georgetown.edu/matlab/>). The integrated intensity at each pinhole was calculated by summing over a square 3 x 3 pixels or 5 x 5 pixels (depending on the magnification of the optics between the EMCCD and the Nipkow disk). A single, uniform, background value was subtracted off - determined by the measured intensity between pinholes - to correct for camera offset and light scattered inside the confocal head. For cell measurements, an intensity threshold was used to select pinholes inside the cell. The threshold was set such that a visual inspection of the selected pinholes coincided with the interior of the cell observed by imaging with the disk spinning. For each investigated pinhole, the 40,000 intensity values per movie were broken into 20 segments, each 2,000 points long, and 20 correlation curves were calculated and then averaged together. Correlation curves from pinholes at the same

location in separate consecutive movies were averaged together. Total acquisition time was typically between 30 seconds and 240 seconds. A nonlinear least-squared curve fit was used to fit the final correlation curves to a model for free diffusion in either three or two dimensions (see below); with an additional additive constant to correct for small, long time scale changes in intensity. The additive offset was typically two or three orders of magnitude smaller than the amplitude of the correlation curve, but its presence led to significantly improved fits - even though other fit parameters were not sensitive to its exact value. Colloidal aggregates or large, transient movements of cellular structures will produce distorted correlation curves that can not be fit by the simple models described below. Therefore, we discarded correlation curves where the sum of residuals to the fit exceeded a threshold value. The threshold was set such that only grossly anomalous curves were rejected. The number of curves rejected by this criterion varied depending on the type of sample under investigation, but was never more than 10% of all measured curves, and was often far less than that.

In an FCS type measurement, the autocorrelation function of intensity fluctuations are computed and are given by [20]:

$$\frac{\langle (I(t) - \langle I \rangle)(I(t + \tau) - \langle I \rangle) \rangle}{\langle I \rangle^2} \equiv G(\tau) \propto \int \Phi(\bar{q}) S(\bar{q}, \tau) d\bar{q}, \text{ where } S(\bar{q}, \tau) \text{ is the dynamic}$$

structure factor of the solution, $\Phi(\bar{q})$ is the Fourier transform of the observation volume, \bar{q} is the wave-vector, and τ is the delay time. If the observation volume is approximated as a three-dimensional Gaussian, then for non-interacting particles diffusion in three dimensions:

$$G(\tau) = \frac{1}{N} \left(1 + \frac{\tau}{\tau_D} \right)^{-1} \left(1 + \frac{1}{S} \frac{\tau}{\tau_D} \right)^{-\frac{1}{2}} \quad \text{(Equation 1, 3D free diffusion)}$$

While for non-interacting particles diffusing in two dimensions:

$$G(\tau) = \frac{1}{N} \left(1 + \frac{\tau}{\tau_D} \right)^{-1} \quad \text{(Equation 2, 2D free diffusion)}$$

N is the average number of particles in the observation volume, τ_D , the diffusion time, is the typical time it takes a particle to diffuse out of the observation volume in the plane of focus, and S is a parameter that measures the elongation of the observation volume

along the axial direction: $S = \left(\frac{w_z}{w_{xy}} \right)^2$ where w_{xy} is the $1/e^2$ width of the Gaussian

observation volume in the XY (focal) plane and w_z is the width of the observation volume

in Z (axial) direction (See Figure 1). Furthermore, $\tau_D = \frac{w_{xy}^2}{4D}$, where D is the diffusion

coefficient of the particle. The brightness of particles was measured by dividing the average intensity at a location by the average number of particles at that location.

FCS

Single point FCS experiments were performed on a custom built setup. The system was constructed around an inverted microscope (Axioinvert 135 invert TV, Zeiss), and a 40x water immersion objective (1.2 NA) was used in all experiments. The excitation light source was the 488 nm or 568 nm line of an Argon-Krypton mixed gas laser (Mells Griot, 35 LTL 835-208). The emission light was split into two beams, which were separately collected by two Avalanche Photodiodes (APD, Pacer Inc, SPCM-AQR-15). The detection apertures were under filled, resulting in an increased observation volume. The output signals were cross-correlated using a dual-channel correlator (Flex-02-12D/B, Correlator.com). This collection procedure results in an autocorrelation curve free from the after-pulsing artifacts which contaminate single APD measurements.

Depending on the type of fluorophore used, the typical excitation power at the sample was in the range of 10 ~ 100 μ W. The total photon number received by a single APD was typically 1 ~ 2 kps. Each sample was measured at least three times, with each individual measurement lasting 15 - 30 second. As in the PACI experiments, correlation curves were fit, using a nonlinear least-squared method, to a model for free diffusion plus an additional additive constant. The system was calibrated with Alexa 488 or Alexa 568, assuming a diffusion coefficients of 400 $\mu\text{m}^2/\text{s}$ [21]. A diffusion coefficient for free dye of 400 $\mu\text{m}^2/\text{s}$ is higher than the typically assumed value of 300 $\mu\text{m}^2/\text{s}$, but it seems more consistent with recent measurements [21]. Errors in the diffusion coefficient used for the calibration will lead to systematic errors in the reported measurements. Using the older diffusion coefficient as a standard, the observation volume was typically determined to be ~1 femtolitre, with $w_{xy} \sim 0.3 \mu\text{m}$ and $w_z \sim 1.5 \mu\text{m}$. The resulting correlation curves were fit using custom written Matlab code.

Sample Preparation

Colloid solutions were cleaned of aggregates by three rounds of sonication, ~10 minutes each, and 5 minutes of centrifugation in a mini centrifuge (National Labnet C-1200). Experiments on colloids and R-Phycoerythrin (RPE) solutions were performed in Lab-Tek II Chambers (#1.5 coverglass, 155409) which were blocked with 10 mg/ml BSA for 30 minutes prior to use.

DiI was incubated with U2OS cells for ~5 min, cells were rinsed to remove excess dye, and imaged immediately. PTEN null 786-O renal cancer cells constitutively expressing an eGFP-FOXO1A fusion were used for the FOXO-GFP experiments. Cells were kept at 37 C by a custom built chamber heating and imaged in phenol red free media.

RESULTS AND DISCUSSION

For imaging applications using a spinning disk confocal microscope, the pinhole and microlens arrays are rotated at ~1,000 frames per second, so the confocal volumes are scanned over the sample multiple times while a single frame is being acquired. Because the pinholes only take up a small fraction of the area of the disk, a given pixel on the camera does not receive light during the majority of time that an image is being acquired.

Thus, stopping the disk from rotating should result in a large increase in the maximum measured intensity. This effect is illustrated in Figure 2, which compares images taken from a homogeneous sample with the disk rotating and stationary. We calculated the integrated intensity at each pinhole by summing over a square 3 x 3 pixels. The mean intensity of pinholes with the disk stopped is 4067 (after background subtraction), compared to a mean intensity of 297 (after background subtraction) for similar sized regions with the disk spinning. Therefore, the detected intensity goes up by a factor of 13.7 when the disk is stopped, and a similar increase in measured molecular brightness should result, greatly facilitating a correlation analysis. We used the PACI setup with a stationary Nipkow disk to perform FCS style measurements.

Measurements on R-Phycoerythrin and Colloids

We first sought to quantify the variability between measurements performed through different pinholes in the spinning disk. We investigated the behavior of R-Phycoerythrin (RPE) in 32% sucrose. RPE is a 250 kD, photosynthetic antenna pigment from red algae, which is commonly used as a label in FACS and flow cytometry because it is stable, water soluble, and extremely bright [22]. The RPE solution is homogeneous, so an ideal measurement would yield identical values of τ_D and N at each pinhole location; however, differing values are obtained in practice. These deviations arise from two sources: 1) an intrinsic differences between locations due to imperfections in the experimental setup and 2) statistical errors in estimating parameters due to the finite time of a measurement. The statistical errors are reduced as the measurement time increases – with a variance inversely proportional to time - while the intrinsic errors are unaffected by increasing the acquisition time. Therefore, we determined the intrinsic differences between pinholes by measuring how the variance in τ_D and N changed with acquisition times. Figure 3A compares correlation curves acquired in 3.8 seconds (left) to curves acquired in 19 seconds (right). The curves acquired in 19 seconds are smoother and the variation between them is smaller. The reduced variation with longer acquisition time can be easily observed by examining the spread in the correlation curves at the shortest lag-time – which is substantially wider for the data acquired in 3.8 seconds. Figure 3B depicts the variance (normalized by the mean squared) of τ_D and N as a function of acquisition time and shows fits to the function: $a/T + E$; where T is the measurement time, E is the intrinsic variance between pinholes, and a is a constant (Figure 3). Taking the square root of E in the two cases reveals that τ_D varies by ~5% between pinholes while N varies by ~7%. These small values indicate that the pinholes are quite uniform.

We attempted to identify other potential sources of systematic error by looking for spatial patterns in results from different pinholes. Figure 4 shows color coded maps indicating the spatial distribution of values of N , τ_D , and particle brightness, at different locations from a solution of 40 nm colloids (obtained by fitting the measured correlation curves to Equation 1). There is no obvious pattern in the distribution of values of τ_D , while N seems to have a tendency to slightly increase towards the periphery (Figure 4). However, the small intrinsic variability of N and τ_D (described above) indicate that any spatial pattern in these parameters is of minor importance. In contrast, the particle

brightness is both significantly more variable, with a normalized standard deviation of 23%, and shows a clear spatial structure (Figure 4, right). These observations are consistent with the pinholes, optics, and alignment being spatially uniform, but an inhomogeneous laser illumination causing the variability in particle brightness. Therefore, care must be taken when attempting to use PACI to measure particle brightness, but results for N and τ_D should not depend on the specific pinhole they are measured through.

The small intrinsic variation between pinholes allows correlation curves obtained at different locations to be averaged when studying homogeneous samples, such as solutions of RPE. Very low noise correlation curves of RPE in sucrose solutions were obtained in ~60 seconds by such averaging, and the resulting curves were fit to Equation 1 (Figure 5A). The model correlation curve provided a good fit to the data because of the limited time scales probed - despite the complex photophysical properties of RPE [23] (and unpublished observations). The viscosity of these sucrose solutions of known concentration was determined from standardized tables [24], and Figure 5B shows that the measured τ_D increases linearly with solution viscosity. This result is expected from the definition of τ_D ($\tau_D \propto D^{-1}$, see above), and the Stokes-Einstein relation, which gives $D \propto \eta^{-1}$, where η is the solution viscosity. Combing data from all solutions of RPE; correcting for the differing viscosities; and using a diffusion coefficient of $39 \mu\text{m}^2/\text{s}$ for RPE in the absence sucrose (measured by FCS, data not shown), yields

$w_{xy} = 0.211 \pm 0.014 \mu\text{m}$. Because we used a comparison with FCS to determine w_{xy} , errors in calibrating the FCS setup will give rise to a bias; thus, if the diffusion coefficient of Alexa 488 is taken to be $300 \mu\text{m}^2/\text{s}$, instead of the recently suggested value of $\sim 400 \mu\text{m}^2/\text{s}$, [21], a value of $w_{xy} = 0.182 \pm 0.012 \mu\text{m}$ results.

We attempted to use fluorescent colloidal particles with nominal diameter of 100nm as an additional standard. We performed dynamic light scattering measurements on these colloids to more precisely measure their size, revealing that their radius of hydration was $r_h = 59 \pm 8.5 \text{ nm}$ corresponding to a diffusion coefficient of $D = 3.7 \pm 0.54 \mu\text{m}^2/\text{s}$. PACI was used to obtain correlation curves from a solution of these colloids, which were averaged over pinholes and fit to a model of one component free diffusion in three dimensions to give $\tau_d = 4.45 \pm 0.43 \text{ ms}$, which implies that $w_{xy} = 0.251 \pm 0.043 \mu\text{m}$. While this calibration to dynamic light scattering data yields a slightly different value of w_{xy} than was obtained by comparison to FCS measurements, they are similar within experimental error. The calibration with dynamic light scattering gives a closer correspondence to the FCS calibration if the diffusion coefficient of small dyes is taken to be $400 \mu\text{m}^2/\text{s}$. Throughout the rest of the text we assume a value of $w_{xy} = 0.211 \mu\text{m}$, but this must be interpreted with caution. Ultimately, the presented measurements are most reliable for relative changes because systematic errors in w_{xy} are difficult to totally correct for (as in standard FCS) [21]; accurate calibrations are required to convert values of τ_D and N to absolute measures of diffusion coefficients and concentrations.

At short lag times, a small but consistent deviation between Equation 1 and the correlation curves for RPE are evident in Figure 5A. While this discrepancy can be

accounted for by the known photo-physical properties of RPE - which can be modeled as a triplet state with a relaxation times of tens of microseconds ([23] and data not shown) - a similar disagreement between measured correlation curves and Equation 1 can result from an incorrectly aligned optical setup [25]. Therefore, we performed additional measurements on a simpler system to better characterize the PACI setup. Figure 6A shows data from a solution of 40nm colloids, obtained in ~5 minutes by averaging results from ~380 separate pinholes. The resulting $G(\tau)$ can be well fit by Equation 1 over four orders of magnitude of correlation, indicating that the confocal volume is well approximated by a Gaussian [25]. Misalignment resulting in a non-Gaussian volume would result in a significant, systematic disagreement with Equation 1. We do observe small, nonrandom deviations with residuals of order 10^{-3} (Figure 6A, lower), which is the magnitude of error expected from approximating the observation volume of a well aligned confocal systems as a three dimensional Gaussian instead of using the full result from diffraction theory [25]. The fit gives $\tau_D = 2.1$ ms, leading to a measured diffusion coefficient of $5.2 \pm 0.3 \mu\text{m}^2/\text{s}$ (assuming $w_{xy} = 0.211 \mu\text{m}$ as described above), which is close to the value of $5.5 \mu\text{m}^2/\text{s}$ expected for spheres of this size. A poorly aligned system will result in an apparent divergence of w_z/w_{xy} [25], whereas our fit yields a reasonable value of 5.6.

We performed an additional test of the shape of the observation volume by measuring the volume with two independent methods. Firstly, we estimated the size of the observation volume by our knowledge of w_{xy} , obtained from calibration with FCS, and w_z/w_{xy} , obtained from fitting the shape of the correlation curve; if the observation volume is assumed to be a three dimensional Gaussian then we can calculate its volume as $V_{\text{gaus}} = \pi^{3/2} w_{xy}^2 w_z = 0.292 \pm 0.034 \mu\text{m}^3$. Secondly, we directly calibrated the observation volume by measuring the average number of colloidal particles at various dilutions with FCS and PACI (Figure 6B). Measurements on free dye of known concentration reveal that the FCS volume was $1.65 \pm 0.29 \mu\text{m}^3$ while the experiments with colloids indicate that the PACI volume is $52\% \pm 20\%$ of the FCS volume: resulting in an observation volume of $0.85 \pm 0.39 \mu\text{m}^3$ for PACI. This directly measured volume is significantly larger than volume calculated assuming a three dimensional Gaussian shape. The apparent discrepancy is most likely caused by the actual shape of the observation volume in a Nipkow disk microscope; a careful theoretical and experimental study has demonstrated that the volume is a Gaussian with long tails – caused by cross-talk between separate pinholes [26]. Such long tails would not be expected to contribute to the shape of the correlation function – which is dominated by the fluctuations from particles moving around the central Gaussian portion - but would result in an effectively larger observation volume as is observed.

Measurements of diI in Cells

We used PACI to measure the diffusion of diI, a fluorescent lipid analog, in cell membranes to illustrate the ability of this technique to probe biologically relevant dynamics in cells. Data was collected from 44 locations at the edge of a U2OS cell in

~90 seconds. Fitting the measured correlation curves to Equation 2 allows τ_D and N to be extracted at each location (Figure 7A). The mean τ_D is 4.6 ms, leading to a diffusion coefficient of $2.4 \mu\text{m}^2/\text{s}$, similar to values previously reported [27]. However, the behavior of diI is highly heterogeneous, and a wide range of τ_D and N were measured in a single cell (Figure 7B), in agreement with the large variability that has been observed in the diffusion of membrane bound dyes in tissue culture cell membranes using ICS performed with an EMCCD and TIRFM [15].

Measurements of Autofluorescent Proteins in Cells

In the previous sections of this paper we demonstrated that PACI can be used to measure the diffusion of 40nm colloids, a highly fluorescent protein complex (RPE), and chemically labeled fluorophores attached to lipid analogs in cell membranes. In this last section we show that PACI can also be used to characterize the dynamics of soluble proteins in cells.

We used PACI to characterize the diffusion of FOXO, a transcription factor, in PTEN null 786-O renal cancer cells stably expressing an eGFP-FOXO fusion protein. The absence of PTEN in this cell line causes constitutively active Akt to phosphorylate FOXO; leading to a cytoplasmic localization of FOXO under our standard imaging conditions. Figure 8A shows fifteen (from a total of eighty nine) correlation curves obtained from a single cell in ~161 seconds. Fitting this data using Equation 1 gives $\tau_D = 1.8 \pm 0.6$ ms, yielding a diffusion coefficient of $D = 6.1 \pm 2.0 \mu\text{m}^2/\text{s}$, comparable to a value of $D \sim 5.2 \mu\text{m}^2/\text{s}$ obtained from standard FCS measurements on these cells (data not shown). This low diffusion coefficient is potentially indicative of FOXO being part of a large complex or engaging in transient interactions with cellular structures. A wide range of τ_D and N were measured within a single cell (Figure 8B). This variability of ~33% (standard deviation/mean) in τ_D and ~24% in N is far greater than can be accounted by artifacts caused by the intrinsic discrepancies between pinholes (see above), and therefore these results are caused by true differences in the behavior of FOXO at different locations in the cell. The measured variation might be caused by changes in underlying cytoskeletal or membrane structures, but more experiments will be required to test that hypothesis.

In most cells there was no obvious pattern to this heterogeneity (Figure 8C). However, on occasion, spatial trends were visible. Figure 9 shows one such example where the measured number of particles gradually decreases towards the edge of the cell. It is not clear what gives rise to this pattern, but it is possible that it reflects the thinning of the cell. If the cell becomes thinner than the observation volume, then a lower measured average number of particles per pinhole will result, even if the actual concentration is uniform. Still, this data demonstrates the ability of PACI to quantitatively measure spatial patterns in the behaviors of soluble proteins throughout cells.

CONCLUSIONS

In this paper we have shown that an EMCCD can be used in conjunction with a stationary spinning disk confocal microscope to simultaneously perform tens or hundreds of FCS style measurements with enough speed and sensitive to quantify biologically relevant dynamics of membrane and soluble molecules labeled with conventional chemical or genetic fluorophores. This approach, which we call pin-hole array correlation imaging (PACI), can be viewed as an intermediate between standard FCS and ICS. PACI has a number of advantages over existing techniques: It can probe time scales hundreds of times faster than is possible with point scanning ICS; the obtained signal to noise is over ten fold greater than ICS performed with a rotating Nipkow disk; unlike ICS with TIRF illumination, PACI can be used to measure the dynamics of molecules away from the coverslip. However, the smallest accessible delay time in PACI is far slower than can be achieved with single point FCS and PACI probes sparser spatial locations than ICS.

There are three factors to consider when deciding whether to use an ICS style analysis with a spinning disk or a PACI style setup with the disk stationary; 1) the time scale of the systems dynamics; 2) the desired spatial resolution; 3) the molecular brightness.

PACI allows faster time scales to be probed because the speed of ICS is limited by the scan rate of the spinning disk. The maximum frame rate that can be achieved with the disk spinning depends on the model of spinning disk and the setup; for the CSU10 and CSUX-1 Basic model the maximum rate is 360 frames/second (or ~30 frames/second if the camera and disk are not synchronized), while for the CSU22 1,000 frames/second can be acquired and 2,000 frames/second can be achieved with the CSUX-1 High-end model. These rates are slower, some substantially slower, than the maximum frame rate of 3,300 frames/second used in this study with the disk stationary.

Conversely, ICS permits more spatial locations to be investigated because the spatial resolution of PACI is limited by the fixed spacing between pinholes on the Nipkow disk. The importance of molecular brightness is more subtle and the relative benefit of the two techniques depends on the characteristics of the sample. Koppel [28], later expanded by Kask, et al [29], analyzed two limiting cases which are helpful to consider; for small molecular brightness, the so called “Poisson noise limit”, statistical noise is dominated by the stochastic nature of the emission and detection of photons, while in the limit of high molecular brightness, the “optimal high-counting-rate limit”, statistical noise is dominated by the number of times molecules move through the observation volume.

In the “optimal high-counting-rate limit” the signal-to-noise ratio of fluorescence correlation measurements are independent of molecular brightness [28, 29]. Therefore, if particles are already very bright with the disk spinning, increasing brightness even further by stopping the disk will not improve the signal-to-noise. Therefore, in this limit, PACI is only advantages if the sampling rate is limited by the disk scan rate.

In the “Poisson noise limit”, which will be relevant to many studies involving fluorescent fusion proteins, the signal-to-noise ratio is proportional to the molecular brightness [28, 29]. Therefore if stopping the disk increases the brightness by a factor of ~14, as we measured, in the limit of low molecular brightness the signal-to-noise will also increase by a factor of ~14. If the system is at steady-state, the same increase in signal-to-noise could be obtained even with the disk spinning by simply collecting data for a longer time period. However, the signal-to-noise increases with the

square root of sampling time [28, 29], so to obtain a similar ~14 fold increase in signal-to-noise would require increasing sampling time by a factor of ~196. This would mean increasing the typical measurement time from ~2 minutes to ~6.5 hours, which might not be practical. Another way to improve the signal-to-noise ratio if the disk is spinning is to average results from different spatial locations [30], but in the “Poisson noise limit” spatial averaging does not offset the reduced molecular brightness associated with spinning the disk. This is because spinning the disk effectively divides the excitation laser among multiple spatial locations by time sharing, so if the number of spatial locations that can be probed increases by a factor of N , the brightness of each spot decreases by a factor of N . However, in the “Poisson noise limit” the signal-to-noise ratio is proportional to the molecular brightness [28, 29] but only increases like the square root of the number of spatial locations [30]. Therefore, spinning the disk and spatially averaging will result in a decrease in signal-to-noise relative to PACI of \sqrt{N} , which from our brightness measurements quoted above we estimate to be $\sqrt{N} \approx \sqrt{14} \approx 3.7$. In summary, ICS is preferable when studying slowly evolving, bright particles with complex spatial structure, such as the cytoskeleton, while PACI is preferable when studying dim samples with rapid dynamics, such as soluble proteins in cells.

There are a number of ways in which the described PACI system could be improved. The current implementation of PACI has a minimum time resolution of ~300 μ s, significantly worse than standard FCS. However, it should be relatively straightforward to reach a time resolution of ~20 μ s - fast enough to measure the diffusion of free dye in water - by covering part of the CCD chip and using the “fast kinetic” readout mode, as has been previously done with an EMCCD and confocal illumination [11]. It would also be beneficial to combine the describe correlation analysis with an analysis of the measured intensities using methods such as photon-counting histogram [31], or the recently developed N&B approach [32], though these will have to be modified to account for the unique noise characteristics of EMCCDs [33] and the inhomogeneous illumination (see above). Finally, it should be possible to develop a two color version of PACI, similar to two color FCS [34], to measure protein binding at multiple locations throughout cells.

ACKNOWLEDGMENTS

We thank David Weitz for support and helpful discussions at the initial stages of this project, Yokagawa for disabling the laser safety, Jagesh Shah for supplying the RPE, and David Miguez for kindly provided the FOXO-GFP cells. Daniel Needleman was supported by Life Sciences Research Foundation, sponsored by Novartis. We thank Tom Kodger for help performing the dynamic light scattering measurements. Single point FCS measurements were performed in the laboratory of Jeremy Gunawardena.

REFERENCES

1. Kim, S.A., K.G. Heinze, and P. Schwille, *Fluorescence correlation spectroscopy in living cells*. Nature Methods, 2007. **4**(11): p. 963-973.
2. Krichevsky, O. and G. Bonnet, *Fluorescence correlation spectroscopy: the technique and its applications*. Reports on Progress in Physics, 2002. **65**(2): p. 251-297.
3. Kholodenko, B.N., *Cell-signalling dynamics in time and space*. Nature Reviews Molecular Cell Biology, 2006. **7**: p. 165-176.
4. Brinkmeier, M., et al., *Two-beam cross-correlation: a method to characterize transport phenomena in micrometer-sized structures*. Anal. Chem., 1999. **71**: p. 609-616.
5. Dittrich, P.S. and P. Schwille, *Spatial two-photon fluorescence cross-correlation spectroscopy for controlling molecular transport in microfluidic structures*. Anal. Chem., 2002. **74**: p. 4472-4479.
6. Digman, M.A., et al., *Measuring fast dynamics in solutions and cells with a laser scanning microscope*. Biophysical Journal, 2005. **89**: p. 1317-1327.
7. Ruan, Q., et al., *Spatial-temporal studies of membrane dynamics: scanning fluorescence correlation spectroscopy (SFCS)*. Biophysical Journal, 2004. **87**: p. 1260-1267.
8. Kolin, D.L. and P.W. Wiseman, *Advances in image correlation spectroscopy: measuring number densities, aggregation states, and dynamics of fluorescently labeled macromolecules in cells*. Cell Biochem Biophys, 2007. **49**: p. 141-164.
9. Peterson, N.O., et al., *Quantitation of membrane receptor distributions by image correlation spectroscopy: concept and application*. Biophysical Journal, 1993. **65**: p. 1135-1146.
10. Wiseman, P.W., et al., *Two-photon video rate image correlation spectroscopy (ICS) and image cross-correlation spectroscopy (ICCS)*. Journal of Microscopy, 2000. **200**: p. 14-25.
11. Burkhardt, M. and P. Schwille, *Electron multiplying CCD based detection for spatially resolved fluorescence correlation spectroscopy*. Optics Express, 2006. **14**(12): p. 5013-5020.
12. Kannan, B., et al., *Electron multiplying charge-coupled device camera based fluorescence correlation spectroscopy*. Anal. Chem., 2006. **78**: p. 3444-3451.
13. Sisan, D.R., et al., *Spatially resolved fluorescence correlation spectroscopy using a spinning disk confocal microscope*. Biophysical Journal, 2006. **91**: p. 4241-4252.
14. Inoue, S. and T. Inoue, *Direct-view high-speed confocal scanner: the CSU-10*, in *Methods in Cell Biology*. 2002. p. 87-127.
15. Kannan, B., et al., *Spatially resolved total internal reflection fluorescence correlation microscopy using an electron multiplying charge-coupled device camera*. Anal. Chem., 2007. **79**: p. 4463-4470.
16. Kolin, D.L., D. Ronis, and P.W. Wiseman, *k-space image correlation spectroscopy: a method for accurate transport measurements independent of fluorophore photophysics*. Biophysical Journal, 2006. **91**: p. 3061-3075.
17. Schwille, P., et al., *Molecular dynamic in living cells observed by fluorescence correlation spectroscopy with one- and two-photon excitation*. Biophysical Journal, 1999. **77**: p. 2251-2265.

18. Adams, M.C., et al., *A high-speed multispectral spinning-disk confocal microscope system for fluorescent speckle microscopy of living cells*. Methods, 2003. **29**: p. 29-41.
19. Crocker, J.C. and D.G. Grier, *Methods of digital video microscopy for colloidal studies*. Journal of Colloid and Interface Science, 1996. **179**: p. 298-310.
20. Ricka, J. and T. Binkert, *Direct measurement of a distinct correlation function by fluorescence cross correlation*. Physical Review A, 1989. **39**(5): p. 2646-2652.
21. Dertinger, T., et al., *Two-focus fluorescence correlation spectroscopy: a new tool for accurate and absolute diffusion measurements*. ChemPhysChem, 2007. **8**: p. 433-443.
22. MacColl, R. and D. Guard-Friar, *Phycobiliproteins*. 1987, Boca Raton, Florida: CRC Press.
23. Hwang, L.C., et al., *Simultaneous multicolor fluorescence cross-correlation spectroscopy to detect higher order molecular interactions using single wavelength laser excitation*. Biophysical Journal, 2006. **91**: p. 715-727.
24. Wolf, A.V., M.G. Brown, and P.G. Prentiss, *Concentration properties of aqueous solutions: conversion tables*, in *CRC Handbook of Chemistry and Physics*, D.R. Lide, Editor. 1979, CRC: Boca Raton, Florida. p. D-270.
25. Hess, S.T. and W.W. Webb, *Focal volume optics and experimental artifacts in confocal fluorescence correlation spectroscopy*. Biophysical Journal, 2002. **83**: p. 2300-2317.
26. Egner, A., V. Andresen, and S.W. Hell, *Comparison of the axial resolution of practical Nipkow-disk confocal fluorescence microscopy with that of multifocal multiphoton microscopy: theory and experiment*. Journal of Microscopy, 2002. **206**: p. 24-32.
27. Bacia, K., et al., *Fluorescence correlation spectroscopy related rafts in model and native membranes*. Biophysical Journal, 2004. **87**: p. 1034-1043.
28. Koppel, D.E., *Statistical accuracy in fluorescence correlation spectroscopy*. Physical Review A, 1974. **10**(6): p. 1938-1945.
29. Kask, P., R. Gunther, and P. Axhausen, *Statistical accuracy in fluorescence fluctuation experiments*. Eur Biophys J, 1997. **25**(163-169).
30. Kolin, D.L., S. Costantino, and P.W. Wiseman, *Sampling effects, noise, and photobleaching in temporal image correlation spectroscopy*. Biophysical Journal, 2006. **90**: p. 628-639.
31. Chen, Y., et al., *The photon counting histogram in fluorescence fluctuation spectroscopy*. Biophysical Journal, 1999. **77**: p. 553-567.
32. Digman, M.A., et al., *Mapping the number of molecules and brightness in the laser scanning microscope*. Biophysical Journal, 2008. **94**: p. 2320-2332.
33. Robbins, M.S. and B.J. Hadwen, *The noise performance of electron multiplying charge-coupled devices*. IEEE Transactions on Electron Devices, 2003. **50**(5): p. 1227-1232.
34. Hwang, L.C. and T. Wohland, *Recent advances in fluorescence cross-correlation spectroscopy*. Cell Biochem Biophys, 2007. **49**: p. 1-13.

FIGURES

Figure 1

A schematic of the experimental setup. The filter cube, and microlense and pinhole arrays (which have been modified to allow laser illumination while not rotating), are inside the spinning disk confocal head. Demagnifying optics were placed between the confocal head and the camera to allow more pinholes to be imaged.

Figure 2

A solution with Alexa 488 (100 nM) imaged with the Nipkow disk spinning (left) and stationary (right). The same laser power, camera settings, and grey scale were used in both pictures, illustrating the higher measured intensities when the disk is stopped (see text). The exposure time was 30 ms.

Figure 3

Measurements on a solution of RPE in 32% sucrose. (A, left) 40 correlation curves measured from different pinholes in 3.8 seconds (blue), with associated best fits (red). (A, right) correlation curves from the same 40 pinhole locations measured in 19 seconds (blue), with associated best fits (red). (B) The variance between pinholes (divided by the mean squared) of measured particle number (N , green) and diffusion time (τ_D , blue) as a function of acquisition time. Both curves were fit to the function $a/T + E$ (red), where E is the intrinsic variance between pinholes, T is the acquisition time, and a is a constant (see text for details).

Figure 4

Color scale maps showing the values of diffusion time (left, with scale in ms), particle number (center), and particle brightness (right, with scale in arbitrary units), at different locations in a homogeneous solution of 40 nm colloids.

Figure 5

PACI measurements obtained by averaging data from different pinholes for solutions of RPE with 0%, 16%, 32%, 40%, 48%, and 56% sucrose. (A) Normalized correlation curves (blue) with best fits to Equation 1 (red). (B) As expected, the measured diffusion time, τ_d , increases linearly with the solutions viscosity, η , (where η_0 is the viscosity of water). Viscosities for sucrose solutions were obtained from [24]. Errors in viscosity were assumed to arise from a one percent error in determining the sucrose concentration (with a linear extrapolation of the viscosities from [24]).

Figure 6

(A, upper) A correlation curve from a solution of 40 nm colloids, obtained in 5 minutes by averaging data from ~380 pinholes (blue) with a best fit to Equation 1 (red). (A, Lower) The residuals to the fit are of order 10^{-3} . (B) A dilution series for 40 nm colloids showing how the measured number of particles changes (FCS in blue, PACI in red). Lines are best fits to the expected linear trend.

Figure 7

The dynamics of labeled diI in the plasma membrane of U2OS cells. (A) 16 representative correlation curves (blue) with best fits to Equation 2 (red). (B) Histograms

of the measured values of diffusion time, (τ_D , left), and particle number (right) obtained from 44 locations in ~90 seconds.

Figure 8

The behavior of FOXO-GFP in tissue culture cells studied with PACI. (A) 15 representative correlation curves (blue) with best fits to Equation 1 (red). (B) Histograms of the measured values of diffusion time, (τ_D , left), and particle number (right) obtained from 89 locations in ~161 seconds. (C) Spatial maps showing the measured mean fluorescence intensity (left) and particle number (right) at different pinholes. The focus is a few microns above the coverslip. Under the experimental conditions FOXO-GFP is predominantly cytoplasmic, and consistent correlation curves could not be obtained from the nucleus. (Scale bar = 10 μm).

Figure 9

FOXO-GFP at the edge of a cell. (A) An image of the cell edge obtained with the Nipkow disk spinning. (B) The disk was stopped and an PACI measurement was performed. The displayed map shows the locations of the pinholes with their color indicating the measured number of particles at that location (scale to right). (C) The measured number of particles at each location as a function of distance along the cell. (D) The measured diffusion time as a function of distance along the cell. (E) Two represented correlation curves from the indicated locations (blue) with the associated best fits to Equation 1 (red).

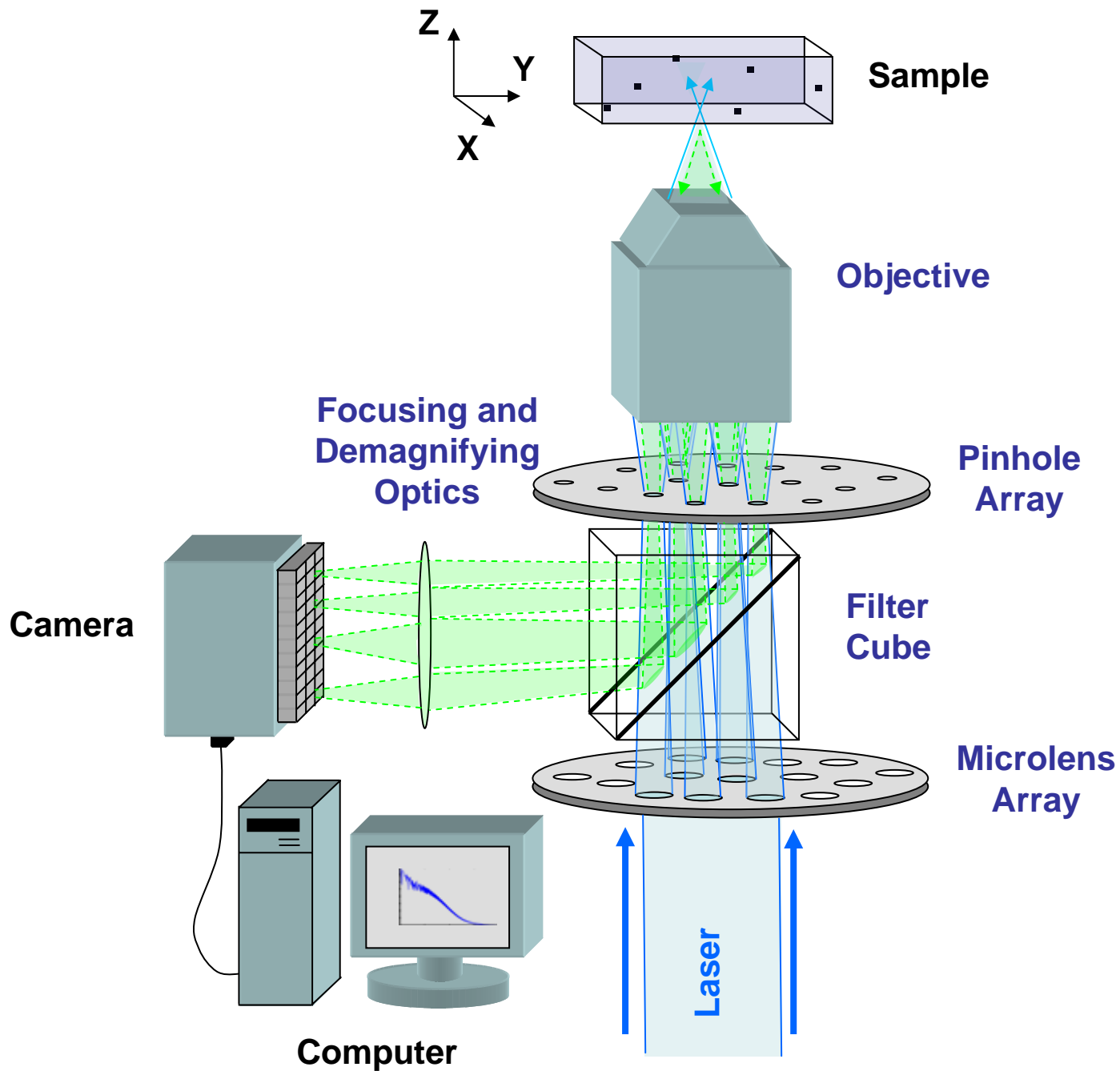
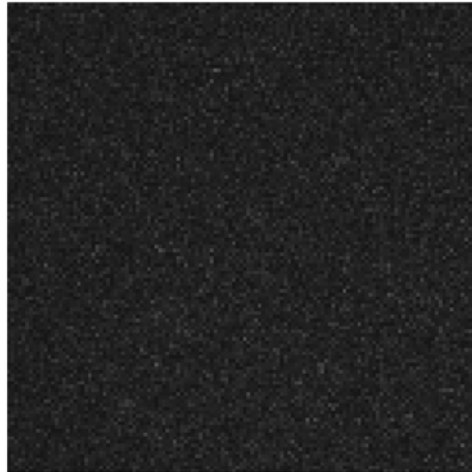


Figure 1

Disk Spinning



Disk Stationary

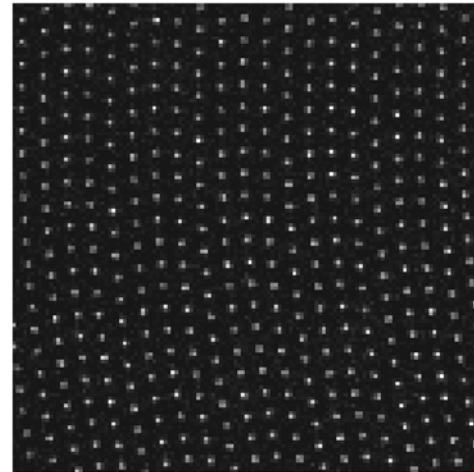


Figure 2

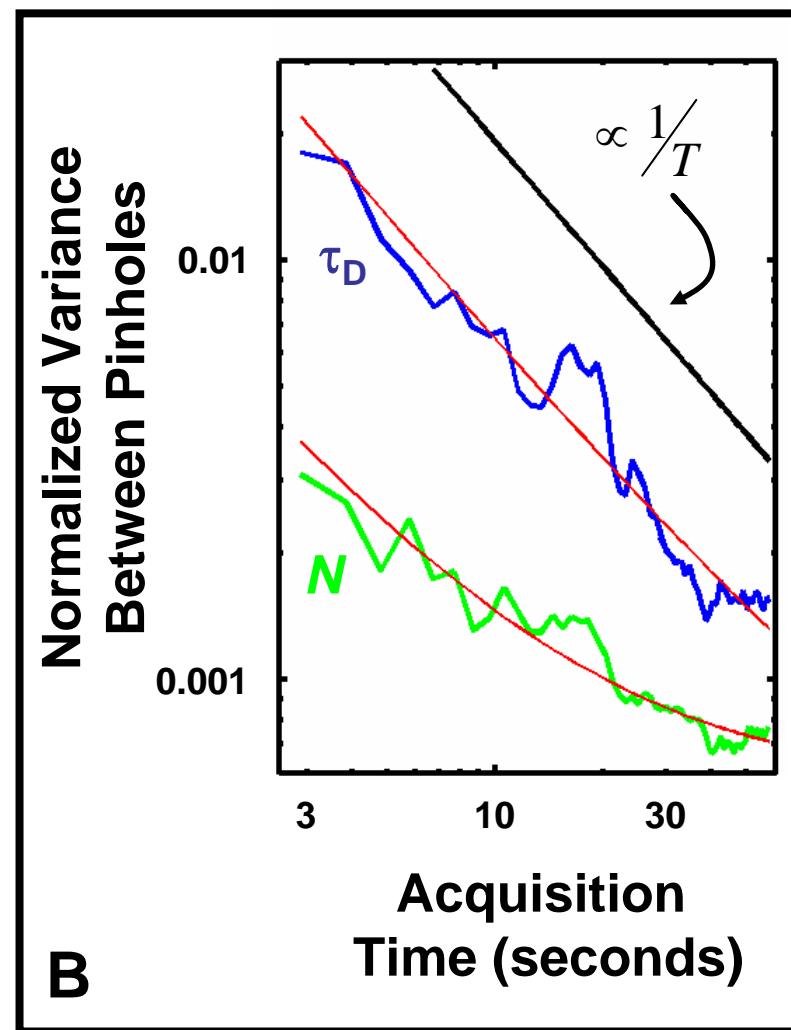
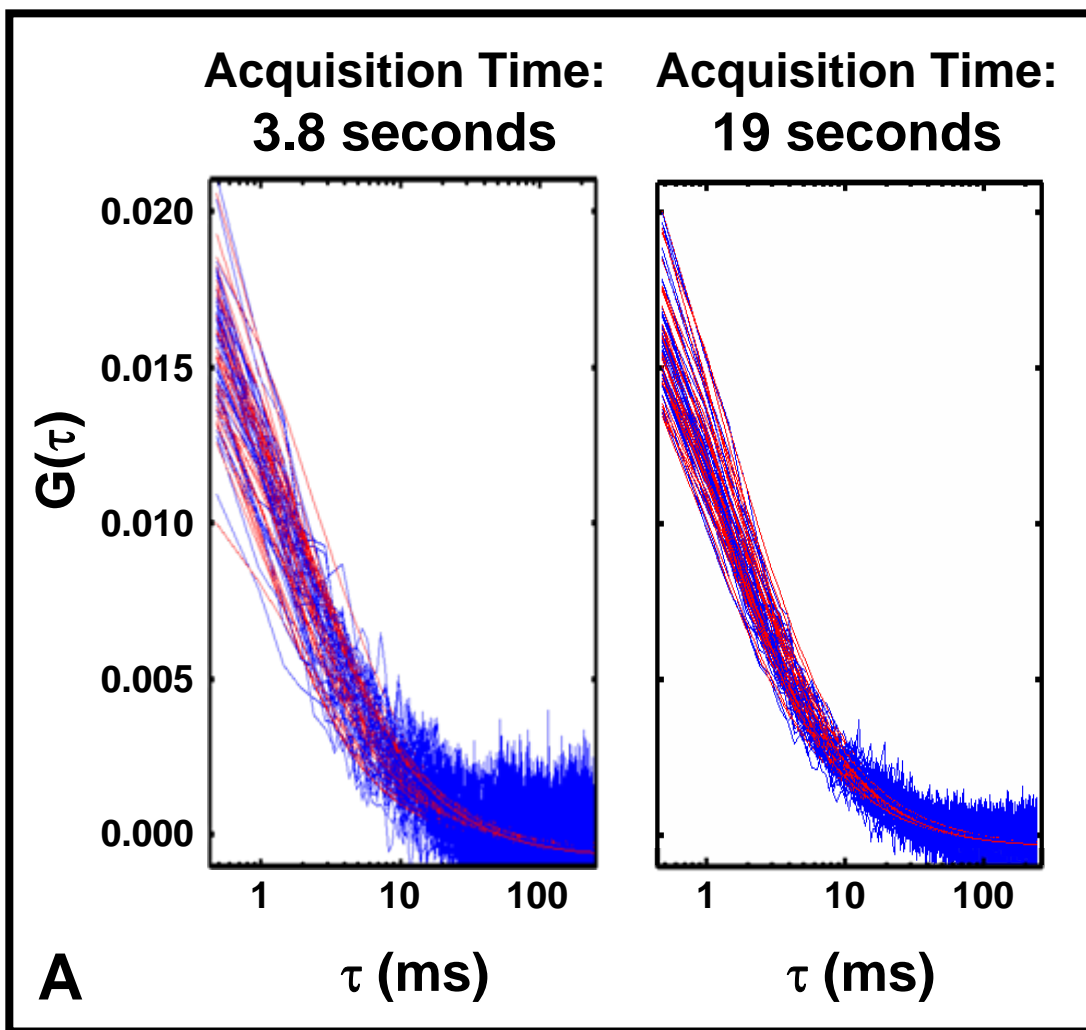
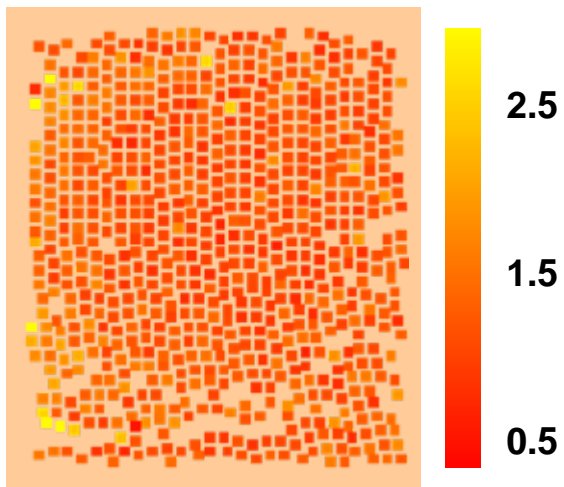
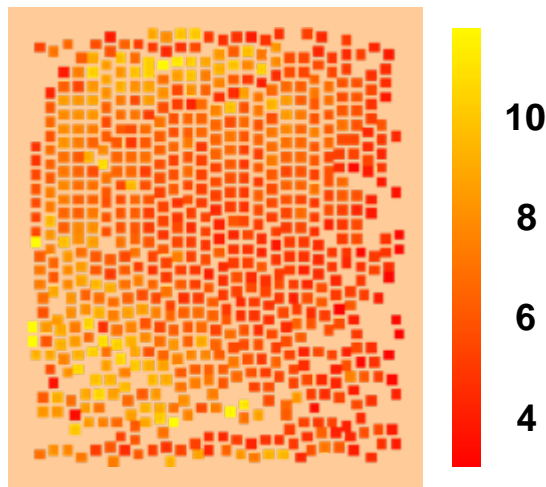


Figure 3

τ_D (ms) Map



Number Map



Brightness (au) Map

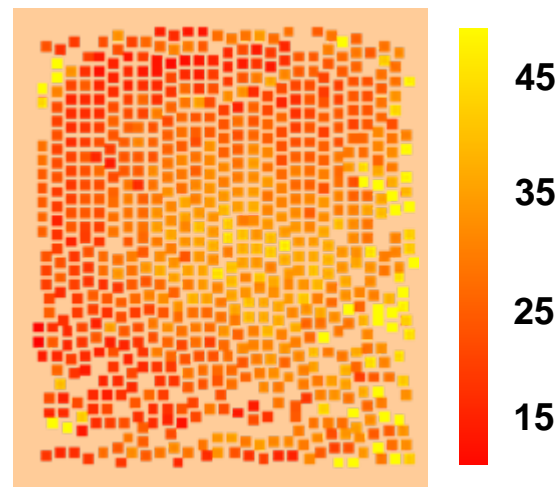


Figure 4

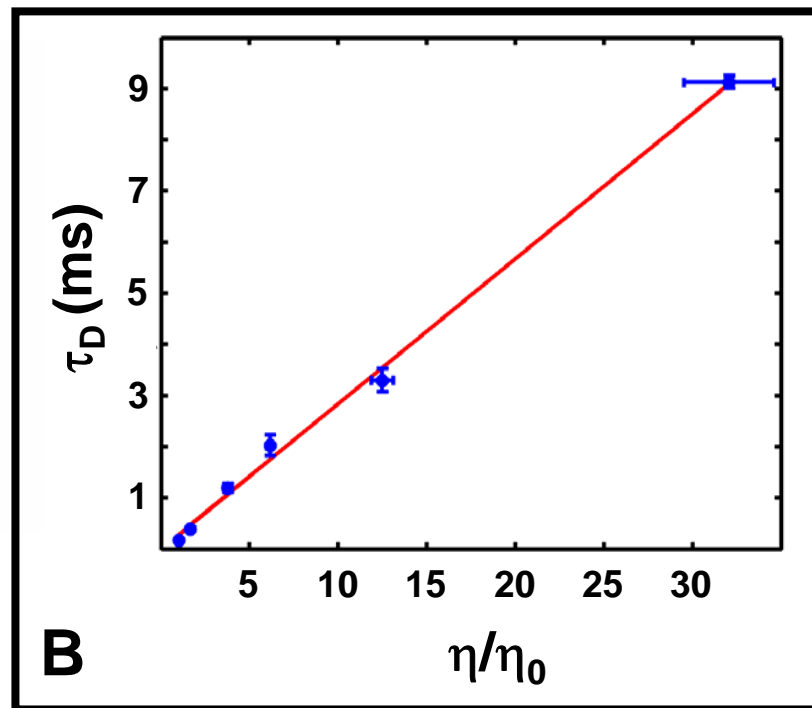
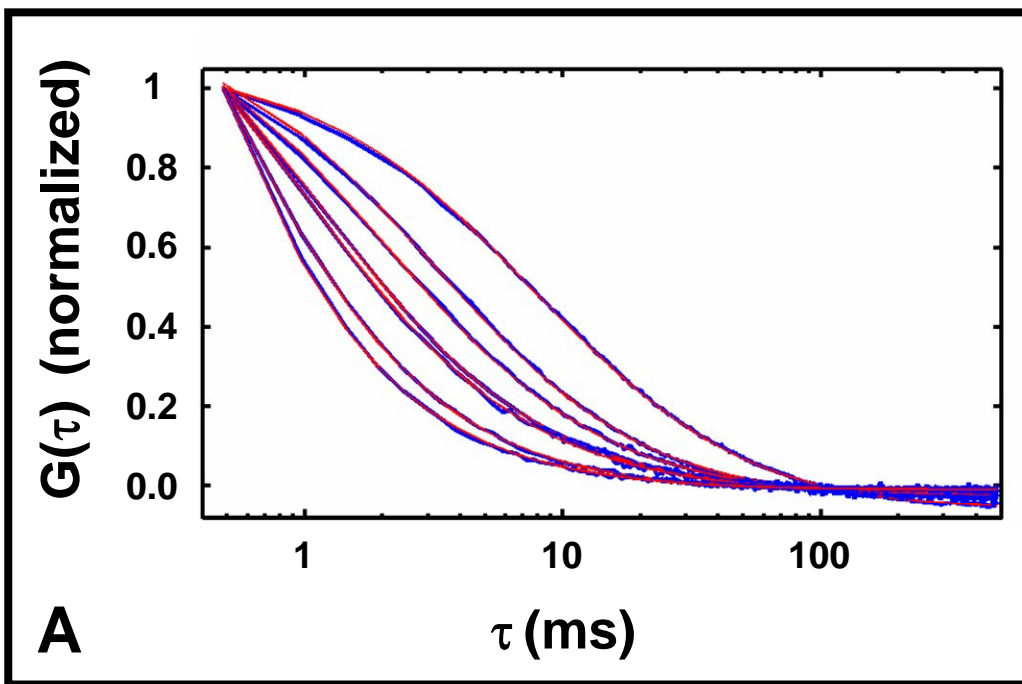


Figure 5

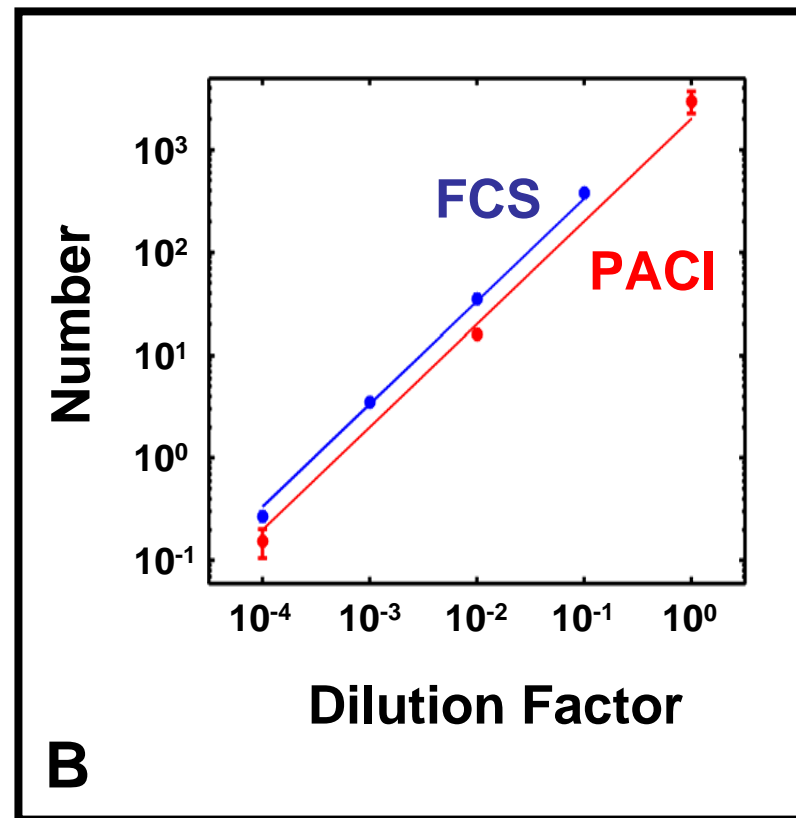
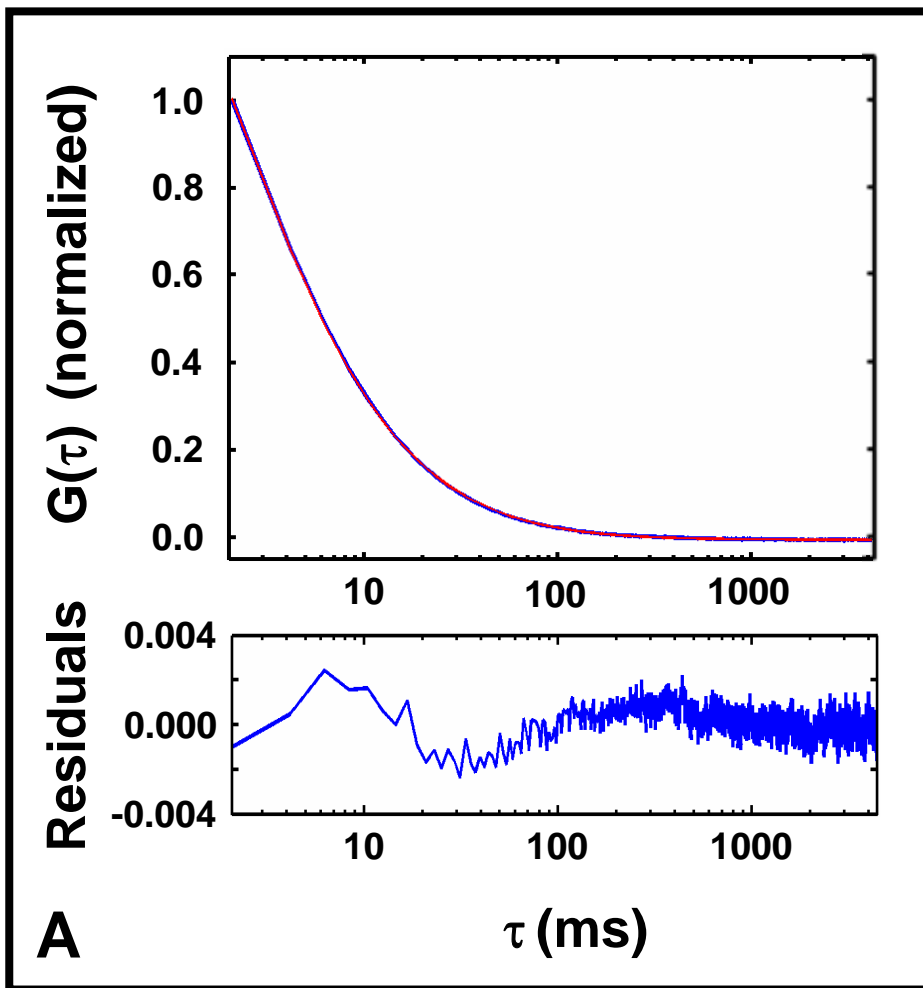


Figure 6

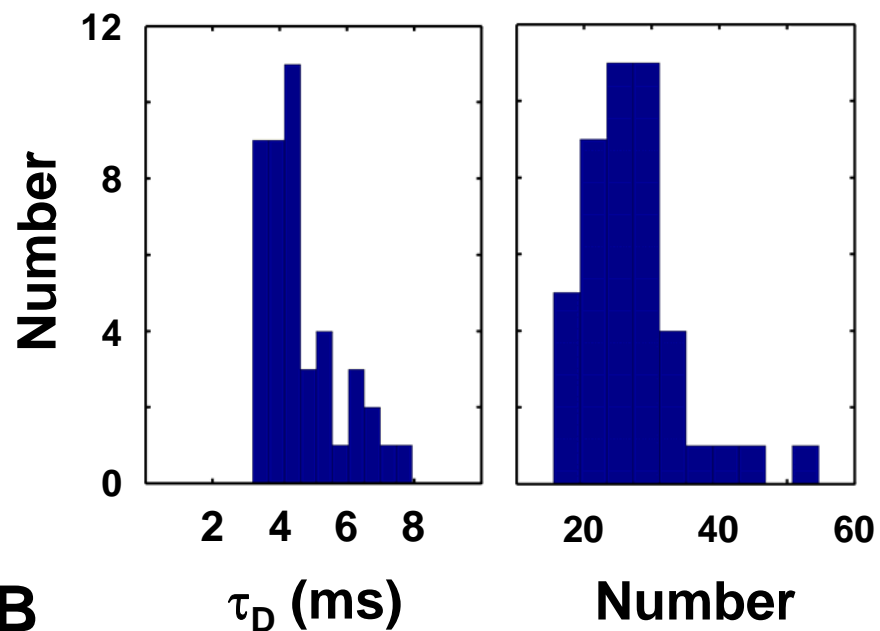
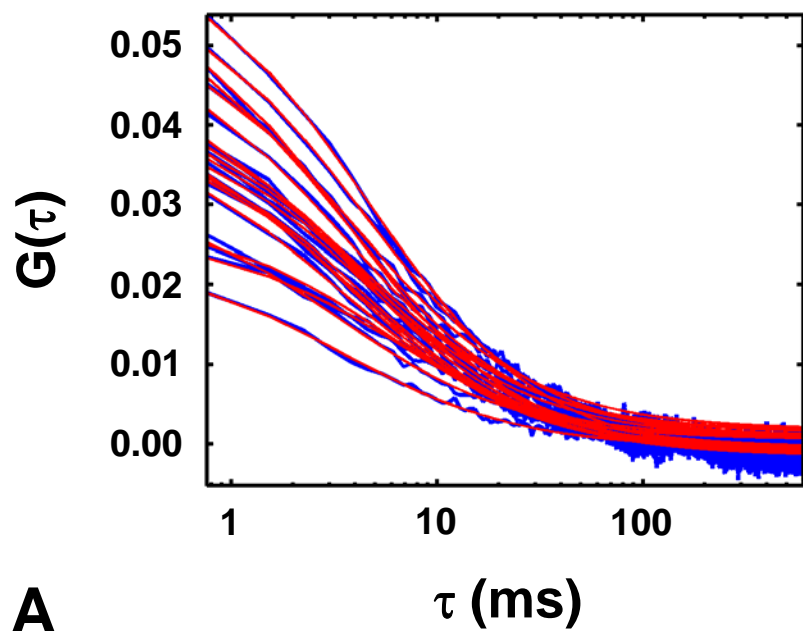


Figure 7

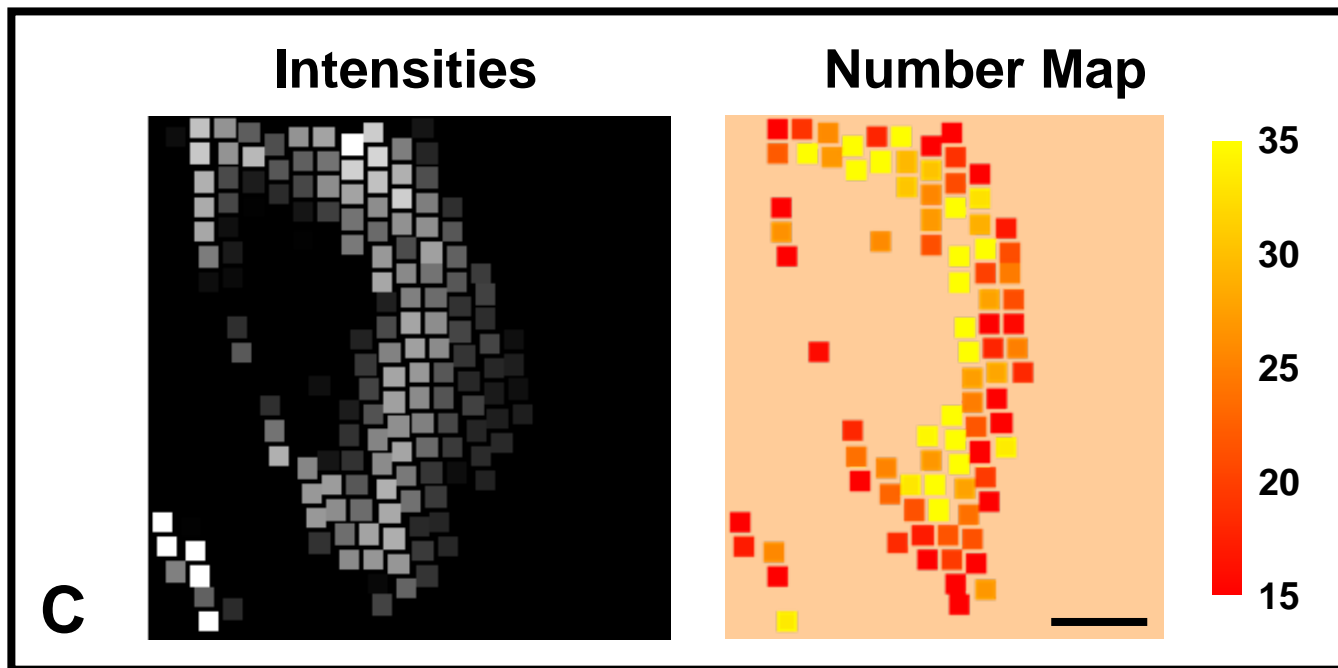
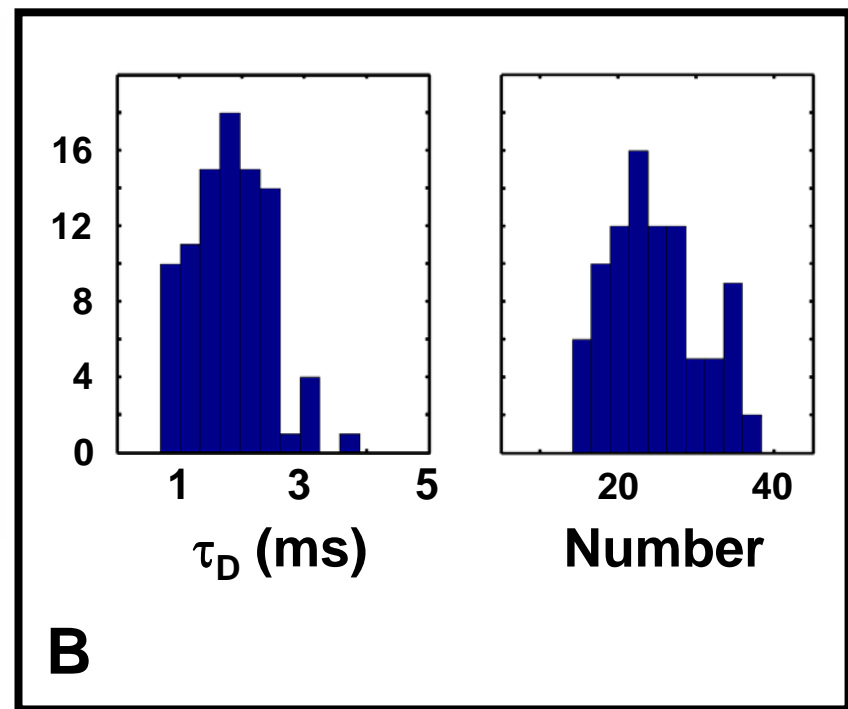
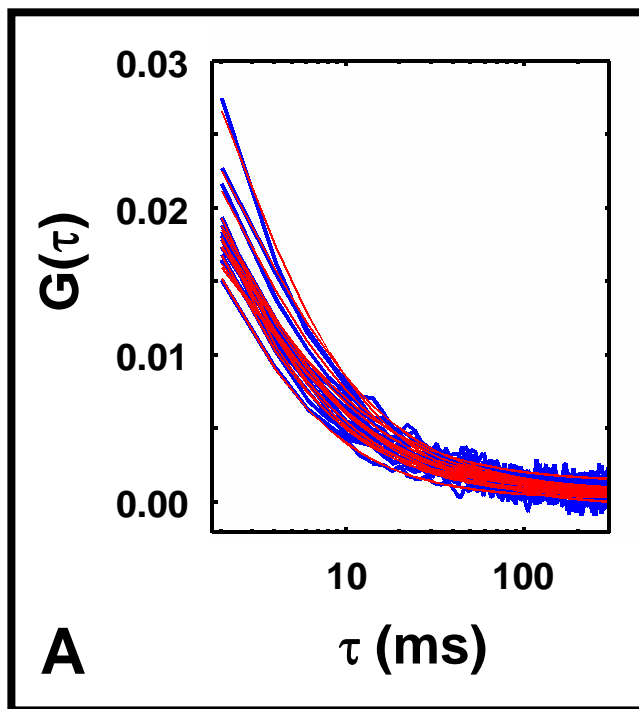


Figure 8

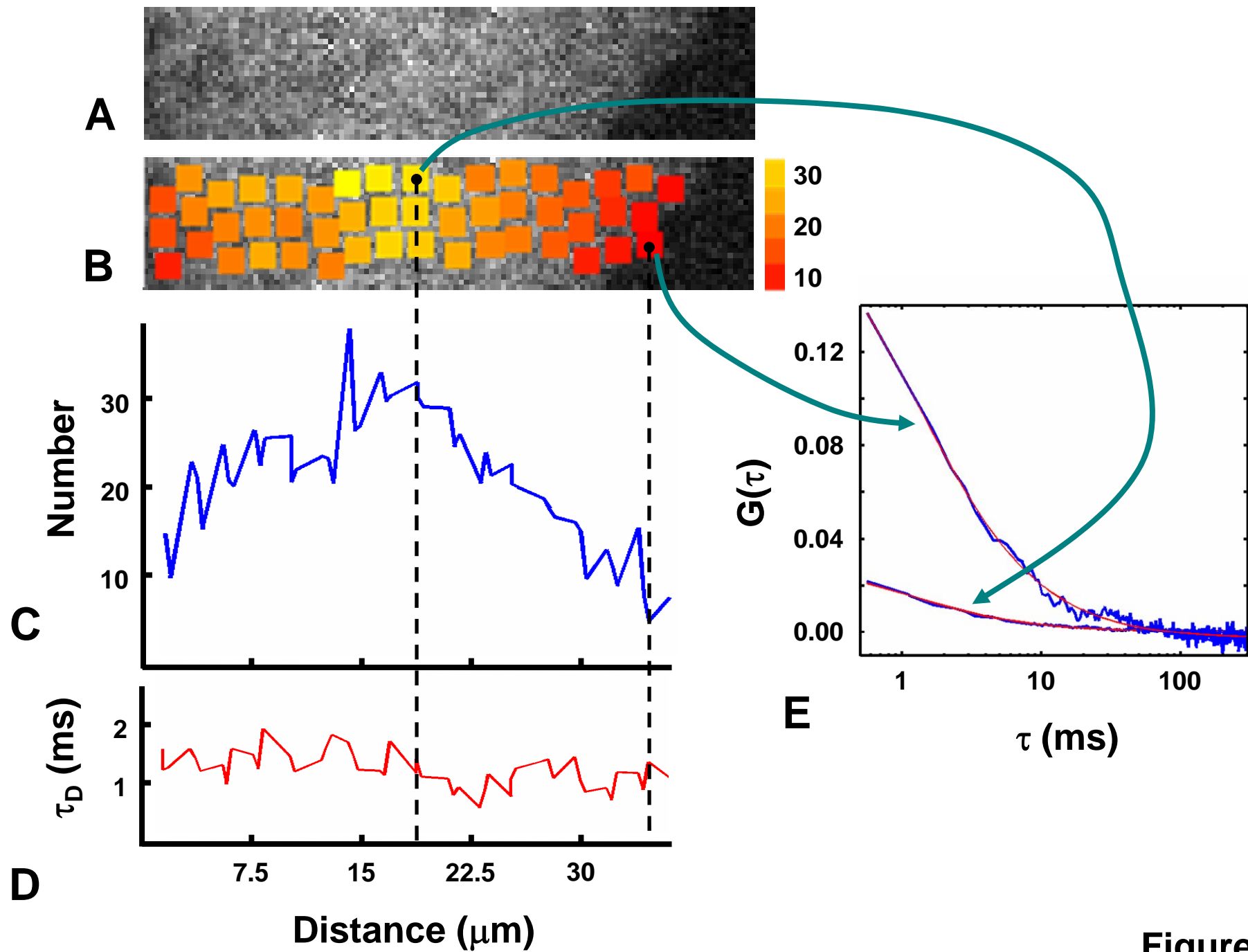


Figure 9